J. Fluid Mech. (2004), *vol.* 509, *pp.* 207–216.
DOI: 10.1017/S0022112004009371 Printed in the United Kingdom

Compressibility effects and turbulence scalings in supersonic channel flow

By H. FOYSI[1], S. SARKAR[2] AND R. FRIEDRICH[1]

[1]Fachgebiet Strömungsmechanik, Technische Universität München, Boltzmannstr. 15, 85748 Garching, Germany

[2]Department of Mechanical and Aerospace Engineering, University of California San Diego, 9500 Gilman Dr., La Jolla, CA 92093-0411, USA

(Received 12 August 2003 and in revised form 25 March 2004)

Turbulence in supersonic channel flow is studied using direct numerical simulation. The ability of outer and inner scalings to collapse profiles of turbulent stresses onto their incompressible counterparts is investigated. Such collapse is adequate with outer scaling when sufficiently far from the wall, but not with inner scaling. Compressibility effects on the turbulent stresses, their anisotropy, and their balance equations are identified. A reduction in the near-wall pressure–strain, found responsible for the changed Reynolds-stress profiles, is explained using a Green's-function-based analysis of the pressure field.

1. Introduction

Wall-bounded compressible turbulence occurs when aerospace vehicles fly at supersonic or hypersonic speeds, both in the external flows over the body and in the engine inlet and combustor. The coupling between turbulence and state variables is a problem of fundamental interest in such flows since the Mach number and temperature changes are typically large. Early experimental evidence on compressible shear flows is discussed by Bradshaw (1977), Fernholz & Finley (1976), and Kline, Cantwell & Lilley (1982) while later experimental and numerical investigations are reviewed by Lele (1994) and Smits & Dussauge (1996).

Supersonic channel flow allows a systematic study of wall-bounded turbulence without other complicating features such as streamwise development, shocks, and flow separation. Coleman, Kim & Moser (1995), by performing direct numerical simulations (DNS) of channel flow between cold isothermal walls with Mach numbers up to $M = 3$, found that Morkovin's hypothesis, 'the flow dynamics follows an incompressible pattern', generally holds. Huang, Coleman & Bradshaw (1995) observed that the turbulent stresses scale with the wall shear stress, τ_w, and semi-local scaling (to be discussed later) is useful. Lechner, Sesterhenn & Friedrich (2001) reported a slight change in Reynolds stresses anisotropy at $M = 1.5$ without giving an explanation.

Compressibility effects on the turbulent stresses are not well understood. In incompressible channel flow, the assumption of $u_\tau = \sqrt{\tau_w/\rho}$ as the velocity scale, and recognition of two length scales, the viscous scale, ν/u_τ, and the half-width h, lead to the well-known inner and outer scalings. Our first objective is to evaluate these scalings in compressible flow where the density ρ and viscosity ν vary. The second objective is to identify changes of turbulent stresses with Mach number.

Case	M	Re	Re_τ	$\frac{L_{x_1}}{h}$	$\frac{L_{x_2}}{h}$	$\frac{L_{x_3}}{h}$	N_{x1}	N_{x2}	N_{x3}	Δx_1^+	$\Delta x_{2_{min}}^+$	$\Delta x_{2_{max}}^+$	Δx_3^+
M0.3	0.3	2820	181	9.6	2	6	192	129	160	9.12	1.02	4.21	6.84
M1.5	1.5	3000	221	4π	2	$4\pi/3$	192	151	128	14.46	0.84	5.02	7.23
M3.0	3.0	6000	556	4π	2	$4\pi/3$	512	221	256	13.65	0.89	9.38	8.91
M3.5	3.5	11310	1030	6π	2	$4\pi/3$	512	301	256	37.89	1.27	13.35	16.85

TABLE 1. Flow and computational parameters.

2. Description of the DNS

The compressible Navier–Stokes equations are solved numerically using the pressure–velocity–entropy formulation of Sesterhenn (2001). The mean pressure gradient, $\mathrm{d}\bar{p}/\mathrm{d}x_1$ is replaced by a uniform body force $\bar{f}_1$. Both channel walls are kept isothermal and are cooled at a temperature of $T_w = 500\,\mathrm{K}$, so that the heat transfer towards the walls allows supersonic fully developed flow. Periodic boundary conditions are used in the stream- and spanwise directions. The compact fifth-order upwind scheme of Adams & Shariff (1996) is used to discretize the hyperbolic (Euler) terms, the compact sixth-order scheme of Lele (1992) for the molecular terms, and a third-order 'low-storage' Runge–Kutta scheme of Williamson (1980) for the time advancement. The numerical algorithm has been previously validated by Lechner *et al.* (2001) whose results for an $M = 1.5$ case agree well with Coleman *et al.* (1995). The mean mass flow rate is increased between cases so that the Mach number, $M = 0.3, 1.5, 3.0$ and 3.5. These cases will be henceforth referred to as M0.3, M1.5, M3.0 and M3.5. Here, $M = u_{av}/c_w$ and Reynolds number $Re = \rho_m u_{av} h/\mu_w$. The bulk-averaged density is defined as $\rho_m = \int_0^h \overline{\rho}\,\mathrm{d}x_2/h$, and u_{av} denotes the Reynolds (rather than Favre) cross-sectionally averaged velocity. The speed of sound, c_w, and viscosity, μ_w, are computed at the constant wall temperature T_w. The friction Reynolds number $Re_\tau = \rho_w u_\tau h/\mu_w$, with $u_\tau = \sqrt{\tau_w/\rho_w}$, is a result of the simulations. Table 1 summarizes the flow parameters, box sizes and numbers of grid points used in the different cases. Equidistant grids are used in (x_1, x_3)-directions and clustering in the wall-normal x_2-direction.

Since Re_τ also increases along with M, the compressible flow results are compared with the incompressible channel flow data of Moser, Kim & Mansour (1999) at $Re_\tau = 180, 395$ and 590, denoted by cases I1, I2 and I3, respectively. Note that the Re_τ values are similar for cases M0.3, M1.5 and I1, and for cases M3.0 and I3. Compressibility effects originate mainly from the large change in fluid properties, $\bar{\rho}$ and $\bar{\mu}$, caused by viscous heating, see figure 1(*a*). Figure 1(*b*) shows that, with the Van Driest transformation,

$$\bar{u}_{1,VD}^+ = \int_0^{\bar{u}_1^+} \sqrt{\bar{\rho}/\rho_w}\,\mathrm{d}\bar{u}_1, \tag{2.1}$$

the mean velocity profile tends towards log-law behaviour, see Coleman *et al.* (1995) for details; however, there are *Re*-associated differences between cases. Smits & Dussauge (1996) report that supersonic boundary layers with moderate pressure gradients show good agreement with incompressible data when transformed according to Van Driest as long as the low-*Re* extent of the inner layer is not too large.

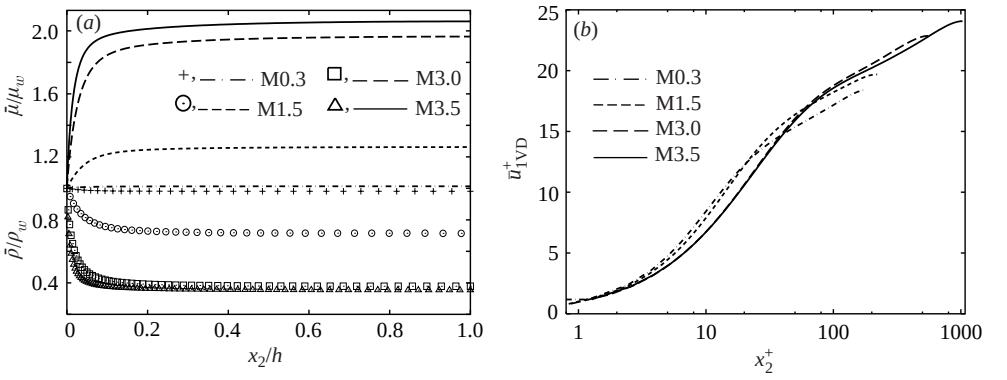

FIGURE 1. (*a*) Variation of mean density (symbols) and mean viscosity (lines). (*b*) Profiles of the Van Driest-transformed mean velocity.

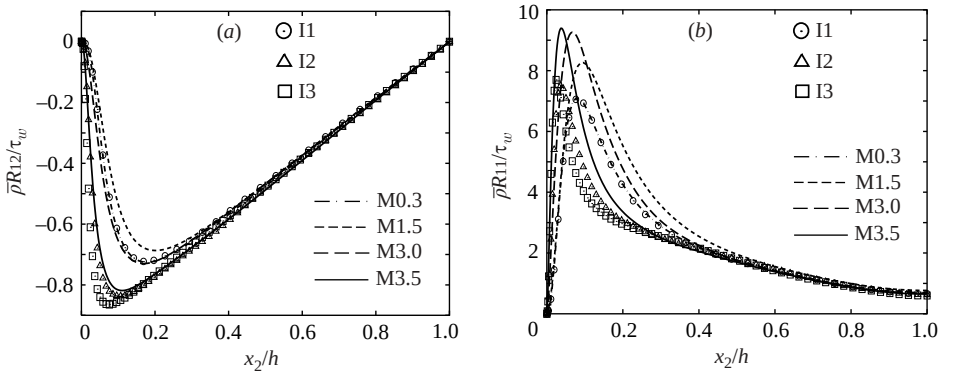

FIGURE 2. Outer scaling of the turbulent stresses, $\bar{\rho}R_{ij}$: (*a*) shear stress, (*b*) streamwise stress.

3. The turbulent stress tensor

In this section, we study the turbulent stress tensor, $\bar{\rho}R_{ij} = \overline{\rho u_i'' u_j''}$, with u_i'' denoting the Favre fluctuation (u_i' denotes the corresponding Reynolds fluctuation).

3.1. *Outer scaling*

Figure 2 shows profiles of the shear and streamwise stresses using outer scaling, that is, using τ_w and x_2/h. Clearly, for sufficiently large x_2/h, compressible and incompressible cases collapse onto a universal profile. This conclusion holds for spanwise and wall-normal components too. (We note that in this, and many other figures, the M0.3 case and the I1 case with similar $Re_\tau = 180$ are practically indistinguishable.)

An explanation of the outer scaling follows after first integrating the $\bar{u}_1$-equation from the wall to obtain

$$\frac{\overline{\mu}}{\mu_w}\frac{\partial \overline{u_1}^+}{\partial x_2^+} - \frac{\bar{\rho}R_{12}}{\tau_w} = 1 - \frac{x_2}{h}, \tag{3.1}$$

where correlations involving viscosity fluctuation, being small, are neglected. Equation (3.1) implies that, when x_2/h is sufficiently large to allow neglect of the viscous stress, $\bar{\rho}R_{12}/\tau_w$ is a linear function of x_2/h. The viscous stresses are taken to be negligible when $x_2^+ > 50$ (equivalently, $x_2/h > 50/Re_\tau$) in incompressible flow so that, with increasing Re_τ, the region with outer scaling thickens. Thus, the shear stress in

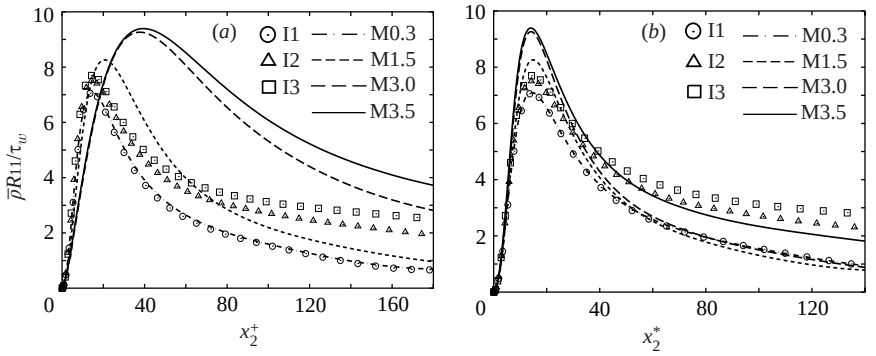

FIGURE 3. Streamwise turbulence, $\bar{\rho}R_{11}$: (*a*) against x_2^+, (*b*) against x_2^*.

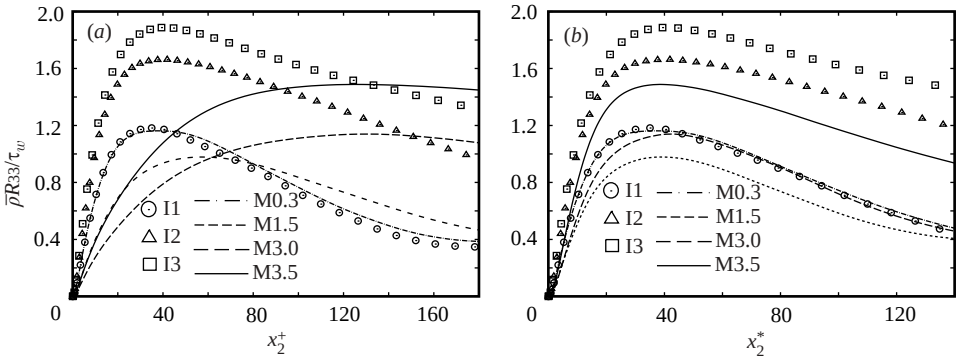

FIGURE 4. Spanwise turbulence, $\bar{\rho}R_{33}$: (*a*) against x_2^+, (*b*) against x_2^*.

case I3 with highest Re_τ shows linear behaviour at the smallest distance, $x_2/h \simeq 0.1$. However case M3.0, at similar $Re_\tau = 560$, shows linear behaviour only for $x_2/h > 0.3$. The temperature increases with increasing x_2, μ correspondingly increases, and the viscous stress in (3.1) remains important for a larger x_2. When $x_2/h > 0.3$, the mean density is almost constant as seen in figure 1(*a*) and, variable density effects being small, the correlation coefficient of $\overline{\rho u_1'' u_2''}$ is practically identical for all cases. From this additional fact we conclude that $\bar{\rho}R_{11}/\tau_w$ and $\bar{\rho}R_{22}/\tau_w$, and finally all Reynolds stresses, tend to a universal dependence on x_2/h sufficiently far from the wall.

3.2. *Inner scaling*

In the incompressible case, inner scaling involves normalization by τ_w and the use of $x_2^+ = x_2 u_\tau/\nu_w$. Such scaling is shown in figure 3(*a*) and figure 4(*a*) for the streamwise and spanwise components, respectively. The higher Re_τ incompressible cases, I2 and I3, although having profiles close to each other as expected, show an increase with Re_τ at large x_2^+. However, cases M1.5–3.5 differ from cases I1–I3 showing that an inner length scale based on wall values is inapplicable.

In the semi-local scaling of Huang *et al.* (1995), while τ_w is still used for normalization, x_2^* replaces x_2^+. Here, $x_2^* = x_2/\delta_\nu^*$ with $\delta_\nu^* = \bar{\nu}/u_\tau^*$ and $u_\tau^* = \sqrt{\tau_w/\bar{\rho}}$, a definition that uses the local viscosity and density. Figure 3(*b*) and figure 4(*b*) show that using x_2^* instead of x_2^+ leads to an improvement; the peak values occur at similar x_2^* in the different cases. However, the peak amplitudes do not collapse. Furthermore, at large x_2^*, the compressible flow profiles are systematically lower relative to cases I2 and I3.

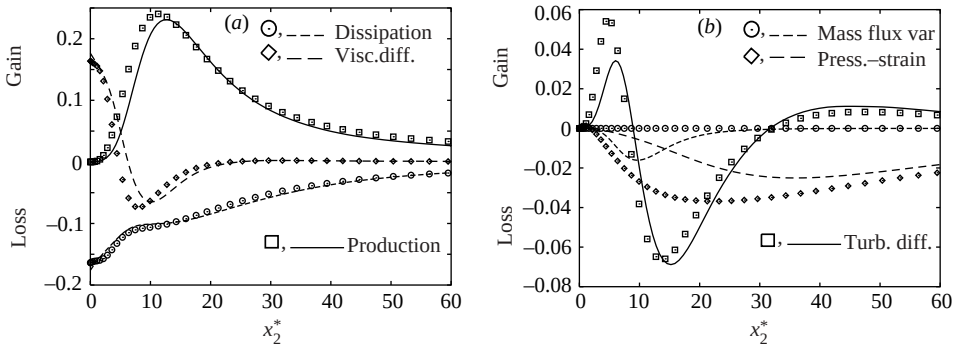

FIGURE 5. Balance of $\bar{\rho}R_{11}$, normalized by $\tau_w^2/\bar{\mu}$, with symbols representing incompressible case I3 and lines case M3.0: (*a*) production, dissipation, and viscous diffusion, and (*b*) pressure strain, turbulent diffusion, and mass flux variation.

We have considered the turbulence transport equations normalized with $\rho_w u_\tau^4/\nu_w$, customary in the incompressible situation, as a function of y^+, finding that case M3.0, when compared with case I3 at similar Re_τ, shows no tendency for collapse. Clearly, an alternative inner scaling is required. Consider the turbulent production, P. Away from the viscous layer, $-\bar{\rho}R_{12} = \tau_w(1 - x_2/h)$, while the mean shear is $\partial\tilde{u}_1/\partial x_2 \simeq u_\tau^*/\kappa x_2$, so that

$$P = \frac{\tau_w^2}{\bar{\mu}\kappa}\left(\frac{1}{x_2^*} - \frac{1}{h^*}\right). \tag{3.2}$$

Equation (3.2) implies that the Reynolds stress budget should be normalized with $\tau_w^2/\bar{\mu}$ and provides additional support for the semi-local coordinate, x_2^*. The balance of $\bar{\rho}R_{11}$ in figure 5(*a*) shows that the dominant terms in the near-wall region, namely the production, dissipation and viscous diffusion, do not differ significantly between cases I3 and M3.0. However, as shown by figure 5(*b*), the pressure–strain correlation,

$$\Pi_{ij} = \overline{p's'_{ij}} = \overline{p'(\partial u_i''/\partial x_j + \partial u_j''/\partial x_i)}/2$$

differs significantly between cases. Since semi-local inner scaling is only a partial improvement over wall-based scaling without giving complete collapse of the turbulence balances, the turbulent stress profiles also do not collapse for incompressible and compressible cases when using x_2^*.

A heuristic explanation of why the local value, $\bar{\rho}$, does not preserve inner scaling follows from the fact that the pressure gradient, ∇p, in the momentum equation is force at a distance. There is a *non-local* relation between pressure and fluid inertia. Mathematically, inversion of the ∇^2 operator in the pressure equation leads to a space integral in the solution. Physically, ∇p at a point P involves momentum per unit volume of the entire turbulent 'eddy' at P whose vertical extent can be estimated using a two-point velocity correlation, taken here to be the wall-normal velocity associated with 'active' turbulence, see figure 6(*a*). Label the two points where $\overline{u_2(x_1, x_2, x_3)u_2(x_1, x_2 + y, x_3)}$, normalized by its maximum, drops below 0.1 as y_- and y_+. Then,

$$\rho_e(x_2) = \frac{1}{y_+(x_2) - y_-(x_2)} \int_{y_-(x_2)}^{y_+(x_2)} \bar{\rho}(y)\,\mathrm{d}y$$

represents the effective density of the fluid volume that influences point P through

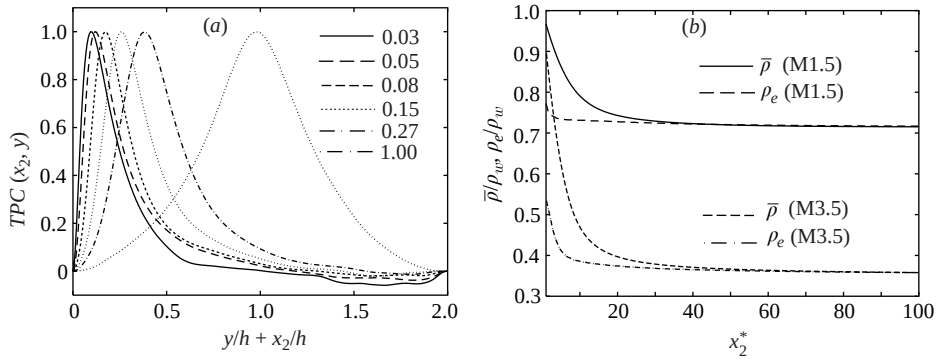

FIGURE 6. (*a*) Wall-normal two-point correlation $TPC(x_2, y) = \overline{u_2(x_1, x_2, x_3)u_2(x_1, x_2 + y, x_3)}$ (case M1.5), normalized by its maximum at six x_2/h values as shown. (*b*) Effective and mean density, normalized by ρ_w.

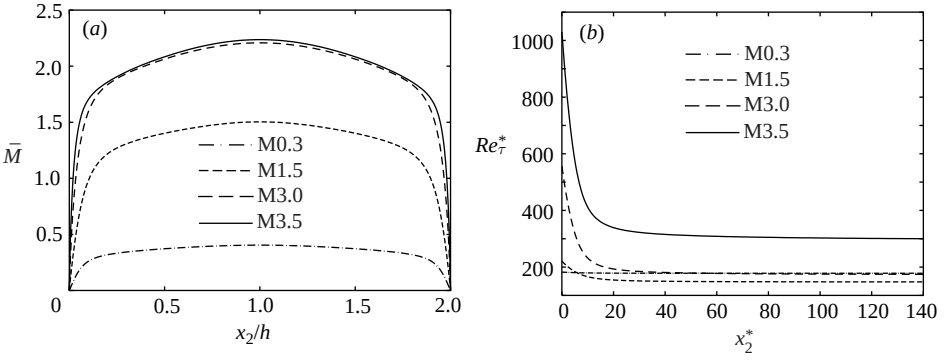

FIGURE 7. (*a*) Local Mach number, $\bar{M} = \bar{u}/\bar{c}$. (*b*) Local friction Reynolds number $Re_\tau^* = \bar{\rho} u_\tau^* h/\bar{\mu}$ plotted against x_2^*.

∇p. Because of the sharp decrease of $\bar{\rho}$ from its wall value followed by a gradual change seen in figure 1(*a*), the effective density is lower than $\bar{\rho}$ near the wall while, in the outer region, ρ_e and $\bar{\rho}$ are almost equal. This is illustrated in figure 6(*b*) for cases M1.5 and M3.5, where $\rho_e(x_2)$ has been calculated by averaging over 20 independent flow realizations. The difference between effective and local mean densities explains why an inner scaling law for turbulence based on local $\bar{\rho}$ fails.

3.3. *Turbulence levels*

Turbulence profiles in the incompressible case depend on the Reynolds number, Re_τ. Comparing cases I1–I3, for instance in figures 3(*b*) and 4(*b*), shows a general increase of all three turbulence intensities with Re_τ over the range covered by DNS. In supersonic channel flow, the Mach number, M, is also important. Another complication is that the local values, $\bar{M}$, and Re_τ^* depend on x_2 as shown in figure 7. Now, case M3.5 has a local $\bar{M}$ profile similar to case M3.0 but the local Reynolds number, Re_τ^*, is significantly larger. The turbulence intensities in case M3.5 are also generally larger, a Reynolds number effect similar to that in the incompressible situation. Let us now turn to compressibility effects. Cases M3.0 and M3.5 in figure 3(*b*) have peak values larger than in case I3 ($Re_\tau = 590$). Since Re_τ^* at the corresponding x_2^* is substantially smaller than 590 this trend cannot be a Re-effect. Now, compare cases M3.0 and

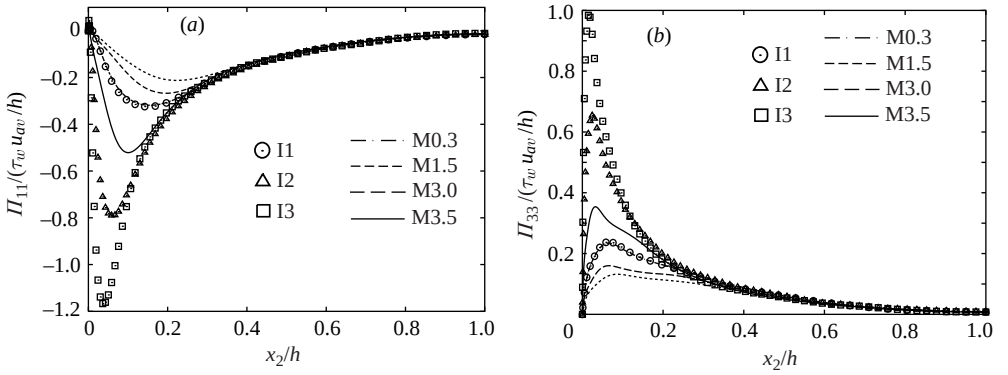

FIGURE 8. The pressure–strain correlation: (*a*) 11-component, and (*b*) 33-component.

M0.3 and notice that, in the region $0 < x_2^* < 40$, the value of Re_τ^* is larger in case M3.0; however, the spanwise intensity in figure 4(*b*) is somewhat smaller in that region, again not a *Re*-effect. It appears that, when M increases, there is an additional effect on near-wall turbulence: the spanwise and wall-normal components of $\bar{\rho}R_{ij}$ are generally smaller than corresponding values in incompressible flow, the streamwise component is larger, and the shear component shows little change. The Reynolds stress anisotropy defined by $b_{ij} = \bar{\rho}R_{ij}/\bar{\rho}R_{kk} - \delta_{ij}/3$ is of interest. Foysi, Sarkar & Friedrich (2003) compared case M3.0 with case I3 having similar Re_τ at the wall finding that, in the near-wall region, the normal stress anisotropies (b_{11}, b_{22}, and b_{33}) are larger in case M3.0, while the shear stress anisotropy, b_{12}, is smaller.

The observed differences between the turbulent stresses can be explained based on their transport equations. For instance, the streamwise balance in figure 5(*a*) shows that the dominant terms do not differ significantly between cases M3.0 and I3, while figure 5(*b*) shows a significant reduction in case M3.0 of the pressure–strain correlation Π_{11}, a sink term in the budget, leading to an increase of $\bar{\rho}R_{11}/\tau_w$ with respect to case I3. In the spanwise balance, the pressure–strain term, Π_{33}, the dominant source, is less in the M3.0 case relative to case I3 in figure 8(*b*), leading to the observed reduction of the spanwise component. The reduction in the wall-normal component (not shown here) is also attributable to the reduction in Π_{22}.

4. Pressure–strain correlation

Although a heuristic explanation for the failure of inner scaling was advanced in § 3.2, a more quantitative explanation based on analysis of the pressure–strain correlation can be constructed as follows.

4.1. *Equation governing the pressure fluctuation*

A starting point is to derive an equation for the pressure fluctuations that is valid for both incompressible and compressible flow. Taking the divergence of the momentum equation, using mass conservation, and, after some algebraic manipulation, we obtain the following equation in channel flow:

$$\nabla^2 p' = \underbrace{-\bar{\rho}(u_i''u_j'' - \overline{u_i''u_j''})_{,ij}}_{\text{A1}} \underbrace{- 2\bar{\rho}\tilde{u}_{1,2}u_{2,1}''}_{\text{A2}} \underbrace{+ \sigma'_{ij,ij}}_{\text{V1}} \underbrace{- 2\bar{\rho}_{,2}(u_2''u_j'' - \overline{u_2''u_j''})_{,j}}_{\text{B1}}$$
$$\underbrace{- \bar{\rho}_{,22}\left(u_2''^2 - \overline{u_2''^2}\right)}_{\text{B2}} \underbrace{- 2\tilde{u}_{1,2}(\rho' u_2'')_{,1}}_{\text{C1}} \underbrace{- (\rho' u_i'' u_j'' - \overline{\rho' u_i'' u_j''})_{,ij}}_{\text{C2}} \underbrace{- \mathrm{D}_{tt}\rho'}_{\text{C3}}. \quad (4.1)$$

Note that the operator $D_{tt} = \partial_{tt} + 2\tilde{u}_j \partial_{jt} + \tilde{u}_i \tilde{u}_j \partial_{ij}$ is Galilean invariant. In incompressible flow, the first two terms on the right-hand side of (4.1), labelled A1 (nonlinear fluctuation), and A2 (mean shear), survive. In compressible flow, there are additional terms, V1 (viscous), B1 (density gradient), B2 (density second-gradient), and the last three terms involving the density fluctuation, C1, C2 and C3.

4.2. *A Green's-function-based solution for the pressure–strain term*

The last term in (4.1), $D_{tt}\rho'$, leads to a convected, inhomogeneous wave equation for the pressure in general. Here, we will neglect terms involving $\rho'/\bar{\rho}$ allowing (4.1) to be interpreted as a Poisson equation for the pressure, and will validate this assumption by comparison of the resulting analytical solution with DNS data.

A Green's-function-based analysis of the Poisson equation for pressure is now performed. The exact wall boundary condition for incompressible flow is $\partial p'/\partial x_2 = \mu \partial^2 u_2'/\partial x_2^2$. In the present case of compressible flow, the dilatation is small and, consequently, the wall boundary condition is given by $\partial p'/\partial x_2 \simeq \mu_w \partial^2 u_2'/\partial x_2^2$. Denote the right-hand side of (4.1) by $\bar{\rho} f'$ and Fourier-transform in the homogeneous (x_1, x_3) coordinates, for example, $p'(x_1, x_2, x_3) \to \hat{p}(k_1, x_2, k_3)$. After introducing (just in the analysis, but not in the figures) a y-coordinate with origin at the channel centreline and normalizing with the channel half-width h, the equation governing the pressure fluctuation becomes

$$\frac{\partial^2 \hat{p}}{\partial y^2} - \left(k_1^2 + k_3^2\right)\hat{p} = \bar{\rho}\hat{f} \qquad \text{with} \quad \left.\frac{\partial \hat{p}}{\partial y}\right|_{y=\pm 1} = \mu_w \left.\frac{\partial^2 \hat{u}_2}{\partial y^2}\right|_{y=\pm 1}. \tag{4.2}$$

The Green's function, $\hat{G}(k, y; y')$ with $k = \sqrt{k_1^2 + k_3^2}$ is the solution of the above equation with $\bar{\rho}\hat{f}$ replaced by the point source, $\delta(y - y')$. We derive the Green's function, $\hat{G}(k, y; y')$, for the homogeneous boundary condition, $(\partial p/\partial y)_w = 0$, using standard methods and find that it is as given by equation (7) of Kim (1989), and also include an additional contribution from the boundary, (4.4) below. The solution of (4.2) is

$$\hat{p}(k_1, k_3, y) = \int_{-1}^{1} \hat{G}(k, y; y')\bar{\rho}(y')\hat{f}(k_1, k_3; y')\,\mathrm{d}y' + \hat{B}(k, y) \tag{4.3}$$

where $\hat{B}$ is given by

$$\hat{B} = \frac{\partial \hat{p}/\partial y|_{y=1} \cosh(k(1+y)) - \partial \hat{p}/\partial y|_{y=-1} \cosh(k(1-y))}{k \sinh 2k}. \tag{4.4}$$

Inverse Fourier transform (4.3) to obtain the pressure in physical space,

$$p'(x_1, y, x_3) = \int_{-1}^{1} \bar{\rho}(y') G * f'(x_1, y, x_3; y')\,\mathrm{d}y' + B'(x_1, y, x_3) \tag{4.5}$$

where the convolution $G * f'$ is the inverse Fourier transform of $\hat{G}\hat{f}$. From (4.5), it follows that the pressure–strain term is given by

$$\Pi_{ij}(y) = \int_{-1}^{1} \bar{\rho}(y')\overline{G * f'(x_1, y, x_3; y')s_{ij}'}\,\mathrm{d}y' + \overline{B' s_{ij}'}. \tag{4.6}$$

The main result of the Green's function analysis, (4.6), makes precise the non-local effect of $\bar{\rho}$ on the pressure–strain correlation. It also helps explain the observed reduction of the pressure–strain term. The fluid in the interior is hotter than that at the cold isothermal walls so that $\bar{\rho}(y')$ is smaller than the wall value ρ_w and, according to (4.6), Π_{ij} is smaller than the corresponding incompressible value.

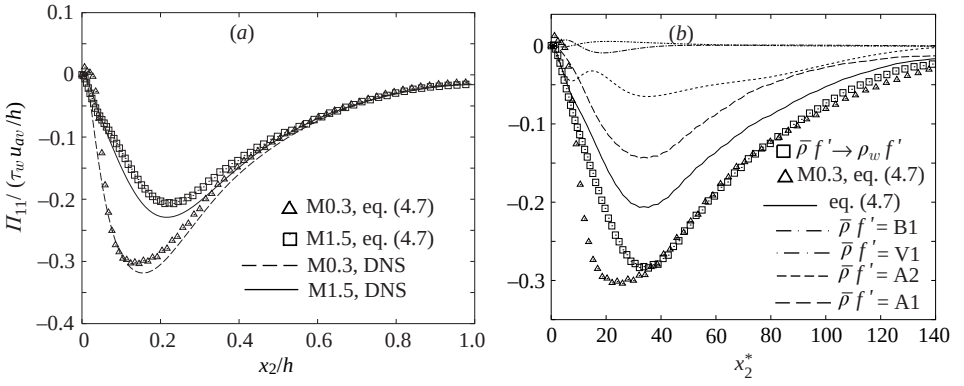

FIGURE 9. (*a*) Comparison of the DNS data and (4.6) for the pressure–strain correlation. (*b*) Symbols illustrate the effect of mean density on Π_{11}. Contribution of different source terms, $\bar{\rho} f'$, to (4.6) in the case of Π_{11} are shown by lines for case M1.5.

The quantity $\overline{G * f'(x_1, y, x_3; y') s'_{ij}}$, a function of y and y', is obtained numerically by Reynolds-averaging the instantaneous values of $G * f'$. Figure 9(*a*) shows a comparison of the analytical solution, (4.6), and the DNS data for cases M0.3 and M1.5. The overall agreement is very good, confirming our *ansatz* that the variable-density extension of the Poisson equation is sufficient for obtaining the pressure–strain term. This is not true in general; in the high-speed shear layer (negligible mean density variation), Pantano & Sarkar (2002) show that the wave operator and consequent impact of finite-time decorrelation of turbulence helps explain the reduction of the pressure–strain correlation in that flow. In channel flow, acoustic contributions lead to a deviation of r.m.s. pressure fluctuations in the outer layer relative to the Green's solution but without affecting Π_{ij}. In order to test that the variation in $\bar{\rho}$ is the main cause of the changed pressure–strain correlation, we take the DNS velocity field of case M1.5 and compute the right-hand side of (4.6) with constant ρ_w instead of the true $\bar{\rho}(y')$ to obtain Π_{11}. The fact that the result (squares in figure 9*b*) compares well with the quasi-incompressible M0.3 case (triangles) in the region $y^+ > 30$ confirms that the reduction in $\bar{\rho}$ with respect to ρ_w is the key to the observed reduction of Π_{ij} in supersonic channel flow. There is an additional change in the region $10 < x_2^* < 30$, presumably because of a difference between the two cases with respect to the velocity derivatives appearing on the right-hand side of (4.6). The right-hand side of (4.6) is evaluated separately with the different sources and plotted as lines in figure 9(*b*) for Π_{11} and case M1.5 and the nonlinear term, A1, is found to be dominant.

5. Concluding remarks

Turbulent stresses, $\bar{\rho} R_{ij}$, in supersonic channel flow with cooled isothermal walls are investigated using DNS with M up to 3.5 and Re_τ up to 1030, compared with incompressible cases, and found to be principally affected by mean property variation, namely the decrease of the mean density and increase of the mean viscosity from wall values. Conventional outer scaling, $\bar{\rho} R_{ij}/\tau_w$ versus x_2/h, collapses all cases considered here in a region sufficiently far from the wall, approximately $x_2/h > 0.35$. Inner scaling with x_2^+ fails. Although using x_2^*, where local $\bar{\rho}$ replaces the wall value, gives better performance, the improvement is only partial because the ∇p term in the momentum equation brings in a non-local dependence on density.

There is a Reynolds number effect in the region $x_2^* > 40$ because Re_τ^*, based on local properties, has a value smaller than the wall value leading to a reduction in turbulence levels relative to those in incompressible flow at the same Re_τ. An additional effect on turbulence in the region of sharp density variation, $x_2^* < 40$ (approximately $x_2/h < 0.15$ in the DNS cases), is linked to reduced pressure–strain correlation, Π_{ij}. A variable-density *ansatz*, neglecting wave-propagation effects, leads to a simplified Green's function solution for the pressure that involves integration over a fluid volume. The effective density of this fluid volume is reduced relative to the incompressible case leading to the decrease of Π_{ij} and consequent increase in turbulence anisotropy. The analytical solution for Π_{ij} agrees well with DNS data. Given the importance of mean density variation, thermal boundary conditions different from those considered here may lead to different changes in the turbulent stresses.

S. Sarkar thanks the Von Humboldt Foundation for financial support.

REFERENCES

Adams, N. A. & Shariff, K. 1996 A high-resolution hybrid compact-ENO scheme for shock-turbulence interaction problems. *J. Comput. Phys.* **127**, 27–51.

Bradshaw, P. 1977 Compressible turbulent shear layers. *Annu. Rev. Fluid Mech.* **21**, 926–927.

Coleman, G., Kim, J. & Moser, R. 1995 Turbulent supersonic isothermal-wall channel flow. *J. Fluid Mech.* **305**, 159–183.

Fernholz, H. H. & Finley, P. J. 1976 *A Critical Compilation of Compressible Turbulent Boundary Layer Data*. AGARDograph 223.

Foysi, H., Sarkar, S. & Friedrich, R. 2003 On Reynolds stress anisotropy in compressible channel flow. *Proc. Third Intl Symp. on Turbulence and Shear Flow Phenomena, Sendai, Japan, 2003* (ed. N. Kasagi *et al.*), Vol. III, pp. 1103–1108.

Huang, P., Coleman, G. & Bradshaw, P. 1995 Compressible turbulent channel flows: DNS results and modelling. *J. Fluid Mech.* **305**, 185–218.

Kim, J. 1989 On the structure of pressure fluctuations in simulated turbulent channel flow. *J. Fluid Mech.* **205**, 421–451.

Kline, S. J., Cantwell, B. J. & Lilley, G. M. (Eds.) 1982 *Proc. 1980-81-AFOSR-HTTM-Stanford Conf. on Complex Turbulent Flows*, vol. 1. Mech. Engng Dept., Stanford University.

Lechner, R., Sesterhenn, J. & Friedrich, R. 2001 Turbulent supersonic channel flow. *J. Turbulence* **2**, 1–25.

Lele, S. K. 1992 Compact finite differences schemes with spectral-like resolution. *J. Comput. Phys.* **103**, 16–42.

Lele, S. K. 1994 Compressibility effects on turbulence. *Annu. Rev. Fluid Mech.* **26**, 211–254.

Moser, R., Kim, J. & Mansour, N. N. 1999 Direct numerical simulation of turbulent channel flow up to $Re_\tau = 590$. *Phys. Fluids* **9**, 943–945.

Pantano, C. & Sarkar, S. 2002 A study of compressibility effects in the high-speed, turbulent shear layer using direct simulation. *J. Fluid Mech.* **451**, 329–371.

Sesterhenn, J. 2001 A characteristic-type formulation of the Navier–Stokes equations for high order upwind schemes. *Comput. Fluids* **30**, 37.

Smits, A. & Dussauge, J. P. 1996 *Turbulent Shear Layers in Supersonic Flows*. American Institute of Physics Press.

Williamson, J. K. 1980 Low-storage Runge-Kutta schemes. *J. Comput. Phys.* **35**, 48–56.